Journal of the European Ceramic Society 37 (2017) 4809–4820

Contents lists available at www.sciencedirect.com

Journal of the European Ceramic Society

journal homepage: www.elsevier.com/locate/jeurceramsoc

Full length article

Macroporous polymer-derived SiO_2/SiOC monoliths freeze-cast from polysiloxane and amorphous silica derived from rice husk

Niloofar Soltani[a,b,c,*,1], Ulla Simon[b,1], Amin Bahrami[a,b,c,1], Xifan Wang[b], Sören Selve[d], Jan Dirk Epping[e], Martin I. Pech-Canul[c], Maged F. Bekheet[b], Aleksander Gurlo[b]

[a] Instituto de Investigaciones en Materiales, Universidad Nacional Autónoma de México, Ciudad Universitaria, 04510 D.F., Mexico
[b] Fachgebiet Keramische Werkstoffe/Chair of Advanced Ceramic Materials, Institut für Werkstoffwissenschaften und – technologien, Technische Universität Berlin, Hardenbergstraße 40, 10623 Berlin, Germany
[c] Centro de Investigación y de Estudios Avanzados del IPN Unidad Saltillo, Ave. Industria Metalúrgica No. 1062, Parque Industrial Saltillo-Ramos Arizpe, Ramos Arizpe, Coahuila, 25900, Mexico
[d] Center for Electron Microscopy, Technische Universität Berlin, Straße des 17. Juni 135, 10623 Berlin, Germany
[e] Institute of Chemistry: Metalorganics and Inorganic Materials, Technische Universität Berlin, Straße des 17. Juni 135/C2, D-10623 Berlin, Germany

ARTICLE INFO

Article history:
Received 26 April 2017
Received in revised form 12 June 2017
Accepted 13 June 2017
Available online 17 June 2017

Keywords:
Polysiloxane
Freeze-casting
Porous ceramics
Rice husk ash
Polymer-derived ceramics

ABSTRACT

A freeze-casting route towards macroporous SiOC/SiO_2 ceramic nanocomposites from preceramic polymers was developed. Amorphous SiOC/SiO_2 monolith with pore channels aligned along the freezing direction were obtained from commercially available methyl-phenyl-vinyl-hydrogen polysiloxane (Silres® H62C) and amorphous silica derived from rice husk ash freeze-cast with water or tert-butyl alcohol, crosslinked and pyrolyzed at 1100 °C in nitrogen. The influence of processing parameters such as solvent (tert-butyl alcohol or water), polymer to silica ratio (2:1, 1:1, 1:2), cooling rate (2, 4, 6 °C/min) and pre-crosslinking of polysiloxane on the porosity and structure of the obtained ceramic nanocomposites were assessed by X-ray tomography, XRD, solid state NMR, scanning electron microscopy and mercury porosimetry. The microstructure of SiOC ceramics derived from the Silres H62C polysiloxane was studied as well.

1. Introduction

Considerable attention has been paid in recent years to the fabrication of macroporous ceramics with controllable pore size and geometry suitable for a variety of emerging applications such as thermal insulation, gas separation, catalysis and bone replacement [1–4]. Defined macroporosity in ceramics is usually created during processing by using replica materials, sacrificial fillers, direct foaming or additive manufacturing techniques [3,5]. Freeze-casting, also known as ice templating, has gained increasing interest in recent years. During freezing, the liquid phase (e.g. water) solidifies and crystallizes and thus acts as a porogen, leaving pores behind after its sublimation [6]. The pore structure of the freeze-cast materials is to a large extent influenced by the processing parameters such as cooling rate and direction, solid content in the formulation, and the final heat treatment [1,6–11]. Solvent in combination with freezing conditions is crucial for defining pore geometry [6,9], i.e. water typically leads to lamellar, camphene and cyclohexane – dendritic, and tert-butyl alcohol – prismatic materials [6,9]. Water-based freeze casting has been most extensively reported in literature, especially for the processing of macroporous oxides such as Al_2O_3, ZrO_2 and zeolites [7,12,13].

Polymer derived ceramics (PDCs), synthesized by the pyrolysis of preceramic polymers such as polysiloxanes, polycarbosiloxanes and polycarbosilanes, is an emerging group of ceramic materials [14]. Tailoring the molecular structure of preceramic polymers offers a wide range of microstructural features that in turn determine the physicochemical properties of resulting PDCs. Adjusting pyrolysis conditions (gas atmosphere, temperature, heating rate) allows for the control over the phase composition, porosity and microstructure of the resulting ceramics [15,16]. One of the main challenges in the processing of PDCs, however, is the high volume shrinkage during the polymer-ceramic transformation. This can be circumvented by the addition of fillers or by modifying the polymer structure [14].

Freeze-casting has rarely been investigated for the processing of macroporous PDCs or their composites [17–21].Since the preceramic polymers are not soluble in or miscible with water,

* Corresponding author at: Circuito Exterior S/N, Circuito de la Investigación Científica, Ciudad Universitaria, 04510, Mexico City, Mexico.
E-mail addresses: niloofar.soltani@iim.unam.mx, nilufar.soltani@gmail.com (N. Soltani).
[1] Contributed equally.

http://dx.doi.org/10.1016/j.jeurceramsoc.2017.06.023
0955-2219/

other solvents such as camphene, cyclohexane and tert-butyl alcohol have been applied for freeze-casting yielding in materials with dendritic and cellular pore geometries. Except the study [19], all aforementioned works utilized either the pre-cross-linked polymers or polymer-derived ceramic powders as, for example, in a recent report about hierarchically ordered micro-meso-macroporous ceramic monoliths freeze-cast from silica sol mixed with a SiOC powder derived from a commercial polysiloxane [22]. To the best of our knowledge, preceramic polymers have not yet been processed with a water-based freeze-casting technique without being pre-cross-linked.

The main goal of the present study is to develop a freeze-casting methodology that allows fabrication of macroporous ceramic monoliths from liquid preceramic polymers. The main emphasis is laid on the processing of amorphous ceramics in environmentally friendly solvents (water) with carbon neutral green additives (silica from rice husk) [23].

2. Materials and methods

2.1. Materials

A commercial methyl-phenyl-vynil-hydrogen polysiloxane (Silres®H62C, denoted as LH62C afterwards, Wacker Chemie GmbH, Germany) was used as received, without further purification. Crosslinking of the polymer – chosen according to the thermal analysis data from [24] – was performed in argon at 250 °C for 2 h with a heating rate of 1 °C/min. The resulting material (labeled as CH62C afterwards) was ground with planetary ball mill PM4 (Retsch, Germany) for 1 h to produce fine powder (≤60 μm sieve grating). Amorphous silica powder derived from rice husk ash was used as a filler. The extraction method of silica from rice husk ash is reported elsewhere [25–27]. Amorphous silica consists of primary loose nanosized particles assembled in a secondary particle agglomerate of approximately 5–10 μm surrounded by a shell, a specific surface area of 150 m^2/g and a density of 1.6 g/cm^3 [28]. Distilled water (W) and tert-butyl alcohol (TBA, $(CH_3)_3OH$, Merck, Germany) were applied as solvents in the freeze-casting process. Dextrin from potato starch (Sigma-Aldrich) and polyvinylbutyral (PVB, $(C_8H_{14}O_2)_n$ Kuraray America Inc., USA) were used as the binders for the water and alcohol containing phase, respectively. Sodium dodecylbenzenesulfonate (DBSS, $CH_3(CH_2)_{11}C_6H_4SO_3Na$, Sigma-Aldrich) was used as an emulsifier in the water-based routes. Polyethylenimine (PEI, $(C_2H_5N)_n$, MW 10.000, 99% purity, Polysciences PEI Inc., USA) and citric acid (CA, $HOC(COOH)(CH_2COOH)_2$, Roth, Germany) were used as dispersants for water-based and TBA-based slurries, respectively.

2.2. Processing

The experimental procedure used in this study is summarized in the flowchart presented in Fig. 1. Table 1 summarizes the experimental parameters varied in this study along with the abbreviations of the specimens. The nomenclature of monoliths was defined based on the type of preceramic polymer (L for LH62C, C for CH62C), ratio of preceramic polymer to silica filler (21 for 2:1, 11 for 1:1, and 12 for 1:2, respectively), and solvent (W for water, TBA for tertbutyl alcohol). Formulations with a total of 30 wt.% loading of preceramic polymer and the amorphous silica filler were stirred in a solvent (W or TBA) with the additives for 4 h. The freeze-casting was performed in a home-made freeze-casting setup that allows for an unidirectional solidification with controlled cooling rates of 2, 4 and 6 °C/min [29]. After the freezing process, all water-based samples were dried in a freeze-dryer (Christ Gamma 2–20, Martin Christ Gefriertrocknungsanlagen GmbH, Germany) at −30 °C under vacuum (0.03 mbar) for ≥3 days. Because the vacuum pump in a freeze-dryer was not equipped with membrane filter for TBA solvent, the Schleck technique was used for sublimation of TBA. After sublimation, the cold samples are carefully removed from the acrylic glass mold. Green bodies fabricated with LH62C polymer were thermally cross-linked by placing them for 2 min in the furnace pre-heated to 300 °C. Finally, all samples were pyrolyzed at 1100 °C under nitrogen atmosphere for 4 h with a heating rate of 3 °C/min. For improving the mechanical strength of the monoliths and to study phase separation processes within the polymer-derived matrix, an additional pyrolysis step at 1400 °C with 3 °C/min for 4 h under argon atmosphere was performed.

2.3. Characterization

Total pore volume and pore size distribution of the whole unbroken monoliths were measured by mercury porosimetry in Porosimeter 2000 WS (Carlo Erba, Italy). To obtain information about the size and orientation of the pores in the scaffolds, X-ray tomography measurements were conducted on unbroken whole monoliths in a home-made setup [30]. The setup consists of a C7942CA-02 flat panel detector (Hamamatsu, Japan) and a L8121-03 microfocus X-ray tube (Hamamatsu, Japan), which was operated at 100 kV. Tomographic reconstructions were computed using VGStudioMAx. The volumetric shrinkage was calculated from the lateral dimensions of the monoliths before and after pyrolysis.

The pore morphology of the monoliths was characterized by Scanning Electron Microscopy (SEM) in a SU8030 microscope (Hitachi, Japan) on the samples cut-off perpendicular to the freezing-direction. The prepared samples for SEM characterization were cut from the same height of all monoliths. Transmission Electron Microscopy (TEM) characterization was performed on a TECNAI $G^2$20 S-TWIN (FEI, Oregon, USA) with LaB_6 electron gun, operated at 200 kV. A Gatan MS794 P CCD camera and DigitalMicrograph software package were used for image recording and evaluation. For elemental analysis, an EDX (EDAX) r-TEM SUTW detector is coupled to the TEM. The samples for TEM characterization were crushed and dispersed in ethanol, then a 3 μl drop was applied on a holey carbon film, supported on a 300 mesh Cu-TEM-grid. The samples were dried in air at 40 °C.

X-ray diffraction (XRD) patterns were recorded on powdered samples in Philips PW 1830 diffractometer operated at 30 mA and 40 kV with CuKα1 = 0.15406 nm radiation with a step time of 10 s and step size of 0.02°. Rietveld refinement was performed using the FULLPROF program [31]. The profile function 7 (Thompson-Cox-Hastings pseudo-Voigt convoluted with axial divergence asymmetry function) [32] was used in all refinements. The resolution function of the instrument was obtained from the structure refinement of LaB_6 standard. Solid state $^{29}Si\{1H\}$ single pulse and MAS cross polarization (CP) measurements were carried out on powdered samples in a Bruker Avance II spectrometer at an external magnetic field of 9.4 T (i.e. a 1H resonance frequency of 400 MHz) using a standard Bruker 4 mm double-resonance H-X MAS probe under MAS rotation of 10 kHz ^{29}Si NMR spectra were fitted with a combination of Gaussian and Lorentzian functions using the procedure of F. Massiot et al. [33].

3. Results and discussion

3.1. SiOC ceramics derived from the Silres H62C polysiloxane

Although Silres®H62C was applied as a preceramic polymer in a number of studies [24,34–45] the structure of the ceramics derived therefrom was not addressed in sufficient detail. This issue hinders a direct comparison of the influence of the silica filler on the struc-

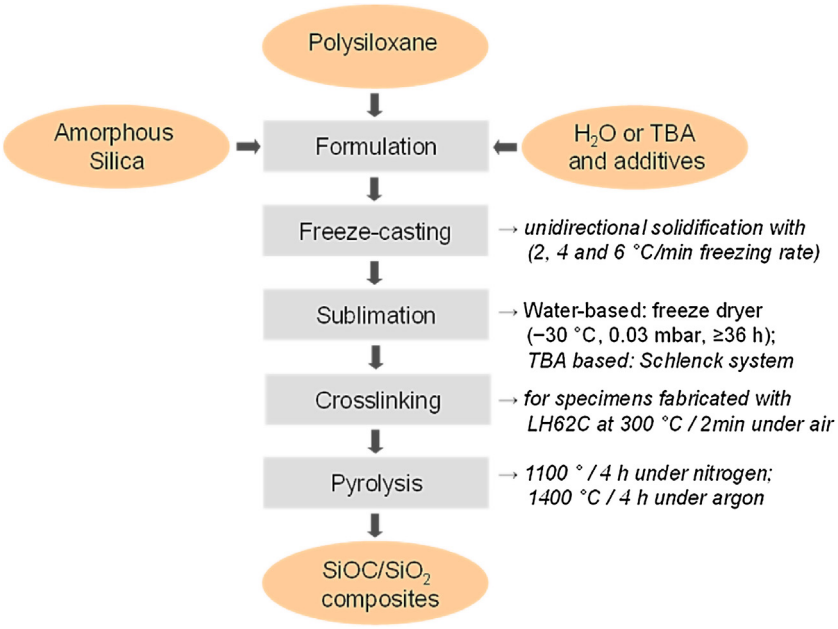

Fig. 1. Flowchart of experimental procedure used for the fabrication of SiOC/SiO_2 macroporous monoliths by unidirectional freeze-casting from polysiloxane and silica from rice husk ash.

Table 1
SiOC/SiO_2 specimens studied in this work.

Specimen	Preceramic polymer[a]	Weight ratio of preceramic polymer to amorphous silica	Solvent	Dispersant[b]	Binder[c]	Emulsifier[d] (wt.%)
C12W	CH62C	1:2	Water	PEI	Dextrin	0.2
C11W	CH62C	1:1	Water	PEI	Dextrin	0.4
C21W	CH62C	2:1	Water	PEI	Dextrin	0.8
C12T	CH62C	1:2	TBA	CA	PVB	–
C11T	CH62C	1:1	TBA	CA	PVB	–
C21T	CH62C	2:1	TBA	CA	PVB	–
L12W	LH62C	1:2	Water	PEI	Dextrin	0.2
L11W	LH62C	1:1	Water	PEI	Dextrin	0.4
L21W	LH62C	2:1	Water	PEI	Dextrin	0.8
L12T	LH62C	1:2	TBA	CA	PVB	–
L11T	LH62C	1:1	TBA	CA	PVB	–
L21T	LH62C	2:1	TBA	CA	PVB	–

[a] liquid (LH62C), cross-linked (CH62C).
[b] PEI (2 wt.%), CA (1 wt.%).
[c] dextrin (5 wt.%), PVB (2 wt.%).
[d] DBSS.

ture of the freeze-cast SiOC/SiO_2 composites. Therefore, in the first step we studied the structure of SiOC ceramics derived from the Silres H62C polysiloxane.

Silres H62C is a highly viscous liquid resin with approximately 42% weight loss in air [45]. At temperature of 250–260 °C reactive Si-vinyl and Si-H bonds undergo thermal cross-linking through hydrosilylation reaction [46]. At temperatures above 1000 °C, under nitrogen flow, the Silres H62C polysiloxane completely transforms to SiO_xC_y ceramics with a weight loss of about 26% [24]. Therefore, for the processing of monoliths we have chosen the following conditions: (a) cross-linking at 250–300 °C; (b) pyrolysis at 1100 °C to produce amorphous ceramics, (c) two-stage pyrolysis, first at 1100 °C followed by 1400 °C to induce the phase-separation and crystallization in the specimens.

Powder XRD reveals that LH62C-derived SiOC sample pyrolyzed at 1100 °C in nitrogen is mainly amorphous with minor amounts of turbostratic carbon (Fig. 2a). Nanocrystalline β-SiC and turbostratic carbon segregate from the SiOC matrix after pyrolysis at 1400 °C. The presence of turbostratic carbon is indicated by the disappearance of (100) and (101) reflections, which are characteristic of the three-dimensional ordering in graphite, and the appearance of a non-symmetrical and two-dimensional reflection of (10) which is the characteristic for disordered sp^2-hybridized carbon [47,48]. These results are consistent with previous works on Silres H62C polysiloxane and other polymer derived SiOC ceramics [49–51]. The Rietveld refinement of the XRD pattern of the LH62C sample pyrolyzed at 1400 °C (Fig. 2b) reveals 26 wt.% of β-SiC with crystallite sizes of 1.5 nm and 74 wt.% of turbostratic carbon with crystallite size 0.7 nm. The average number of graphite stacking layers, which was estimated from d_{002} and crystallite size along the c-axis (L_c) [52], is found to be 1.9. The absence of any crystalline SiO_2 phase after pyrolysis at such high temperatures shows the characteristic high-temperature stability of polymer-derived ceramics, which can be attributed to the presence of free carbon nanodomains. In fact, carbon can act as a diffusion barrier to the atomic rearrangement and restrict the domain size of tetrahedral SiO_4 units which remains lower than the critical size required for the nucleation of SiO_2 phase [53].

The crystallization and phase-separation processes observed in the LH62C-derived SiOC are confirmed by the TEM characterization.

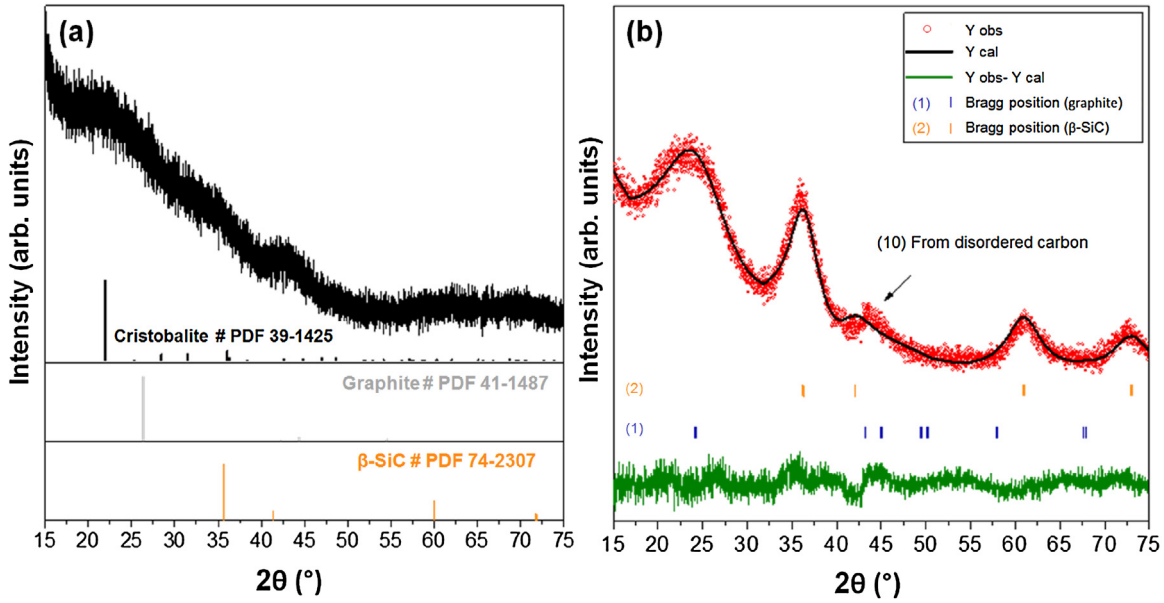

Fig. 2. LH62C-derived SiOC specimens: (a) XRD pattern of LH62C-derived SiOC specimen pyrolyzed at 1100 °C; tick marks refer to Bragg reflections of α-cristobalite, graphite and β-SiC; (b) Rietveld refinement of the XRD pattern of the LH62C-derived SiOC sample pyrolyzed at 1400 °C, showing observed (red circles), calculated (black solid line) intensities and difference (green solid line). Tick marks refer to Bragg reflections of graphite (1) and cubic β-SiC (2). The large difference between observed and calculated intensities at 2θ ~44° is due to the disappearance of (100) and (101) reflections characteristic of the 3D ordered graphite, and the appearance of non-symmetrical two-dimensional reflection (10) which is the characteristic for disordered sp^2-hybridized carbon. (For interpretation of the references to colour in this figure legend, the reader is referred to the web version of this article.)

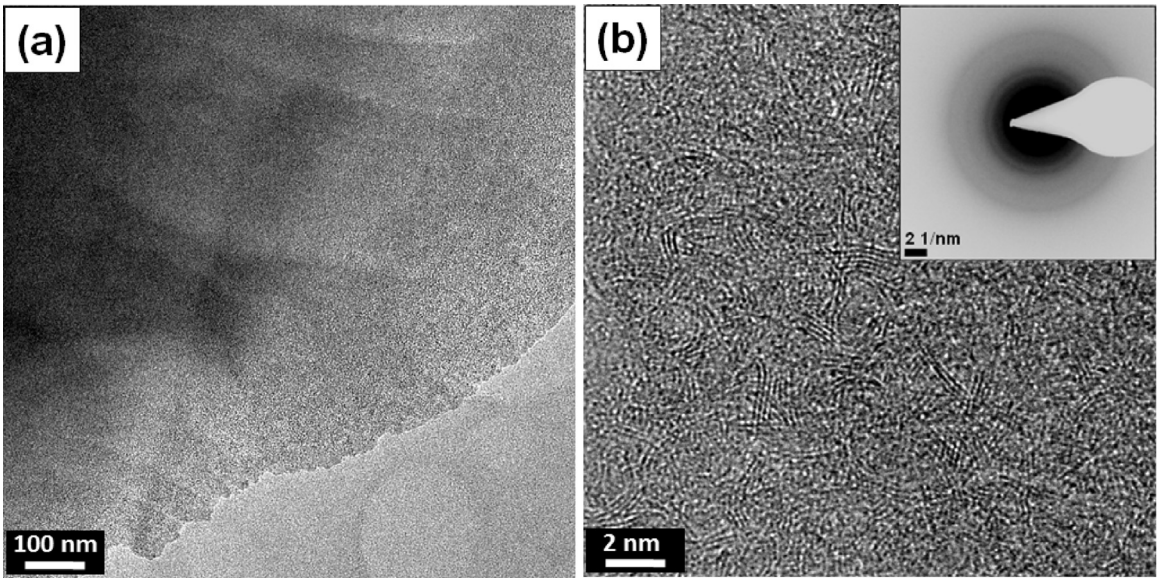

Fig. 3. TEM images and diffraction pattern (inset in b) of LH62C-derived SiOC ceramic pyrolyzed at 1100 °C confirm the homogeneous amorphous matrix with embedded worm-like turbostratic carbon precipitates.

The TEM images of LH62C pyrolyzed at 1100 °C display characteristic worm-like turbostratic carbon precipitates embedded in the amorphous SiOC matrix (Fig. 3). This result agrees with XRD characterization (see Fig. 2a) and the finding reported previously [5].

The pyrolysis at 1400 °C induces phase-segregation and crystallization within the SiOC matrix. The dark-field image, presented in Fig. 4a, shows the formation of nano-sized crystals in the amorphous matrix. High-resolution TEM (Fig. 4b) confirms the presence of nano-sized SiC crystallites (shown in white squares 2–4) with a measured interplanar distance of approximately 0.25 ± 0.01 nm which corresponds to the [25] of β-SiC and was confirmed by Fourier-transformation and electron diffraction analysis (see Fig. 4 and Table S1). In addition, a high-volume fraction of the turbostratic carbon with crystallites of a few nanometers in size are proven (interplanar distance of 0.34 nm, shown in white square 1). The estimated crystallite sizes from TEM, agree with XRD results, which give for β-SiC and turbostratic carbon 1.5 nm and 0.7 nm, respectively.

Further insight into the SiOC microstructure is provided by solid-state ^{29}Si-NMR characterization, which demonstrates significant difference in the silicon environment in the LH62C-derived SiOC samples pyrolyzed at 1100 and 1400 °C. The characteristic peaks at chemical shifts of −114 and −14 ppm correspond to SiO_4

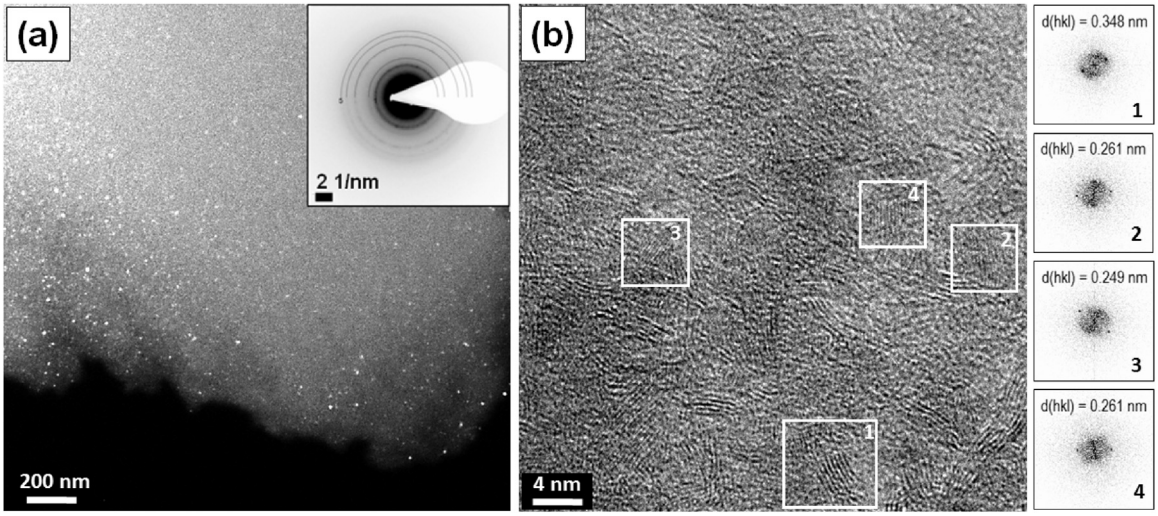

Fig. 4. TEM images of LH62C-derived SiOC specimen pyrolyzed at 1400 °C: a) dark field image displays tiny nanocrystallites in an amorphous matrix and diffraction pattern (inset) shows crystalline β-SiC (see Table S1 for details), b) HR-TEM images confirm β-SiC (squares 2–4) and turbostratic carbon (square 1). The insets show Fourier-transformed high-resolution TEM data for β-SiC (2–4) and turbostratic carbon (1).

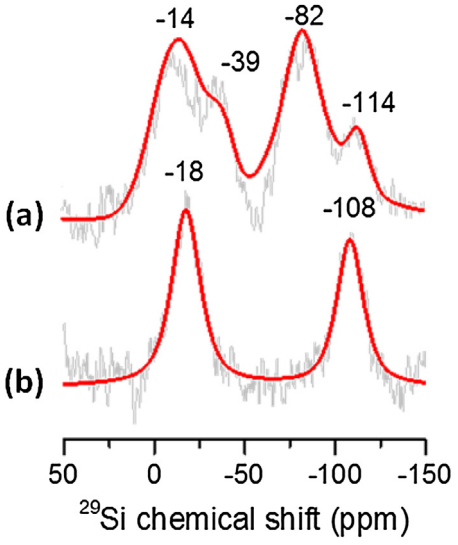

Fig. 5. Solid-State $^{29}Si\{^{1}H\}$-NMR spectra of the LH62C-derived SiOC specimens pyrolyzed at 1100 °C (a) and 1400 °C (b). See the text for the interpretation of the spectra.

and SiC_4 units and −82, −39 to different kinds of oxygen-rich SiC_xO_{4-x} [54,55], were observed for the specimen pyrolyzed at 1100 °C. The specimen pyrolyzed at 1400 °C demonstrates chemical shifts at −108 and −18 ppm, which correspond to SiO_4 and SiC_4 units. Peaks at −82 and −39 ppm, which could be assigned to mixed-bond units such as SiO_3C and SiO_2C_2, are not present in this specimen. This result fully agrees with the XRD and TEM studies pointed at the phase-separation of amorphous SiOC matrix to crystalline β-SiC and amorphous SiO_2 (Fig. 5).

3.2. *Freeze-cast SiOC/SiO_2 monoliths*

The monolithic green bodies freeze-cast from LH62C polysiloxane without filler do not stay form-stable and begin to flow after the sublimation of the solvent (water or TBA). Therefore, to form-stabilize the freeze-cast monolithic green bodies the amorphous silica is added as a filler to preceramic polymer. Alternatively, we study another route in which the LH62C polysiloxane is thermally cross-linked before freeze-casting and then mixed with amorphous silica. As very brittle specimens were obtained in this route, the main emphasis is laid on the processing of amorphous ceramics from liquid LH62C polysiloxane and amorphous silica derived from the rice husk ash. Therefore, the pyrolysis temperature is set to 1100 °C, only in exceptional cases the pyrolysis is performed at 1400 °C to study the effect of phase-separation on the stability of monoliths. To make the process more environmentally friendly, water-based route is also investigated.

The form-stabilization of green-bodies (Fig. 6) as well as a significant reduction of volume shrinkage (Fig. 7) is achieved for specimens with amorphous silica filler starting from the weight ratio of polymer to silica 1:1. Form-stabilization is further improved and shrinkage further reduced by increasing the silica content and by using water instead of TBA as a solvent. The shrinkage is further reduced by applying the crosslinked polymer; however, as these specimens are very brittle and their fabrication requires an additional step and a similar processing route was recently reported [22], in the next sections we mainly focus on the characterization of the specimens fabricated from liquid polymer, that is LH62C-based samples.

As the shrinkage is significantly reduced in the specimens freeze-cast with amorphous silica starting from the weight ratio of polymer to silica 1:1, in the next step these materials are analyzed in more detail, i.e. especially the influence of the solvent (water or TBA), cooling rate (2, 4 and 6 °C/min), and the polymer crosslinking on the pore geometry and the microstructure of the specimens is addressed. As the main interest was to fabricate macroporous amorphous specimens, the emphasis was laid on the samples pyrolyzed at 1100 °C. Here, one must notice a main difference between TBA- and water-based freeze-casting processing. In the former silica particles are dispersed in the solution of polysiloxane in the TBA; in the latter, the silica particles are dispersed in the microemulsion of polysiloxane in water. These specimens were not homogeneous due to the foaming effect of the emulsifier (DBSS). Despite this difference, the influence of the parameters stated above is similar for both processing routes and can be summarized as follows: (i) an increase in the cooling rate reduces the pore size, and (ii) the use of the cross-linked polymer (i.e. CH62C-derived specimens) results in particulate walls that destabilize the monoliths. Both solvents – TBA and water – allow for the fabrication of pore channels oriented along the freezing direction.

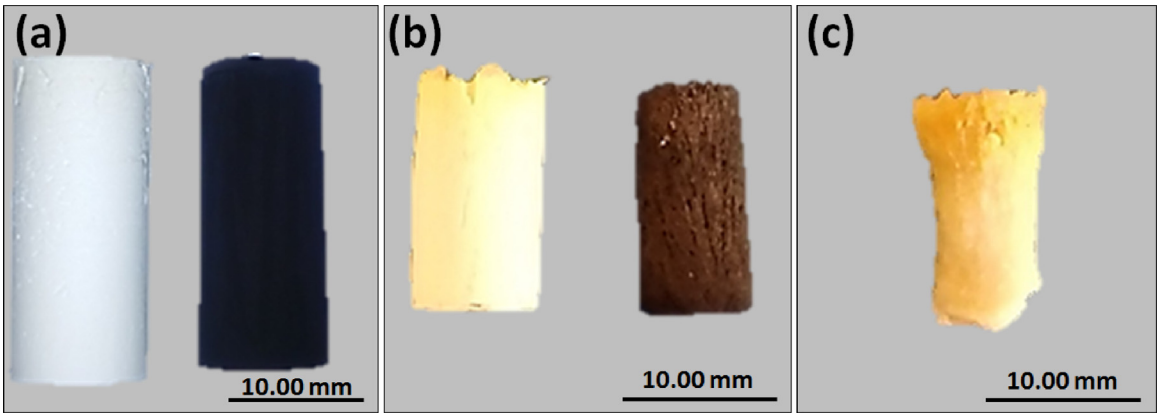

Fig. 6. Photographs of C11W (a), L11T (b) and L21T (c) monoliths frozen at 2 °C/min. Left images display green-bodies after sublimation of a solvent (a) followed by thermal cross-linking (b, c); right images display the specimens pyrolyzed at 1100 °C. The L21T monolith was not form-stable and was destroyed during the pyrolysis.

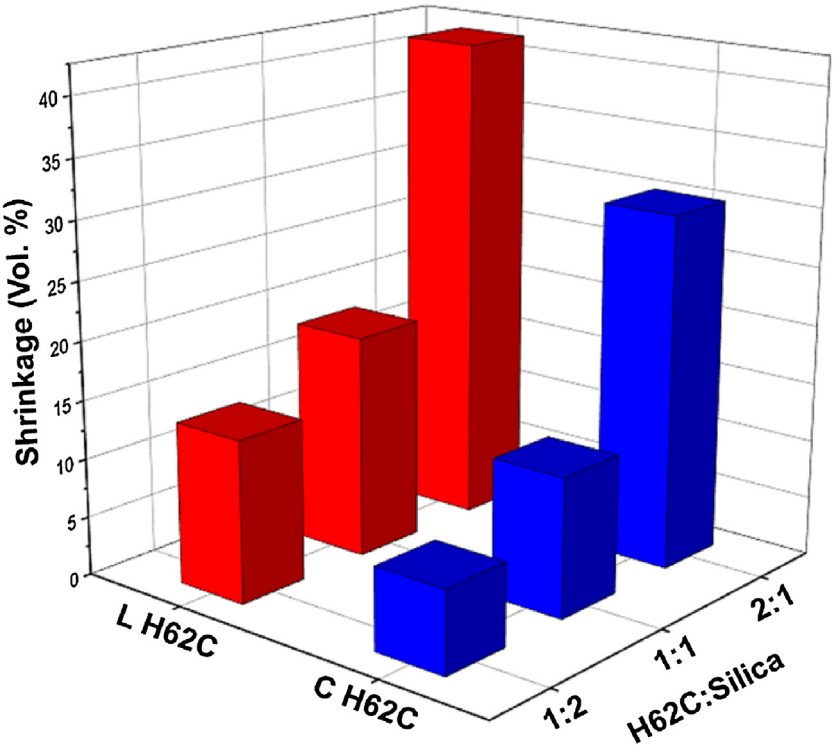

Fig. 7. Volume shrinkage of the LH62C- and CH62C-derived $SiOC/SiO_2$ monoliths fabricated in water at 4 °C/min and pyrolyzed at 1100 °C.

Some representative examples of the monolith fabricated with TBA and water are given below along with the most significant features and peculiarities. Fig. 8 displays the X-ray micro-tomogram and SEM images confirming hexagonal-like (prismatic) pore channels in the L11T samples solidified in the TBA. This specimen displays columnar pores (at the top of the specimen), intermediate and dense (at the bottom of the specimen) structures. This is a typical feature of the ceramics fabricated by unidirectional freeze-casting. The initial TBA crystals nucleated in the cold region – close to the cold copper surface at the bottom of the specimen – are randomly oriented and the growth velocity is high enough to entrap all the particles, leading to a dense microstructure at the bottom part of the monolith [11]. At the intermediate positions the pores are oriented randomly. At the top the alignment of the pores along the freezing gradient is observed. The hexagonal form of the pores is similar to that previously observed in YSZ ceramics frozen with TBA and is due to the hexagonal packing of TBA crystals [56].

A decrease in the cooling rate enhances the pore radius and reduces the total pore volume (Fig. 9). For example, the L11T specimen frozen with 6 °C/min displays a broad pore radius distribution in range of 3–>50 μm with a median radius pore radius of 16.3 μm and a total intruded pore volume of 1719 mm^3/g. An additional contribution of tiny pores around 0.005–0.05 μm is observed, which is caused by pores within the walls. By reducing the cooling rate from 6 to 2 °C/min the median radius pore radius increases from 16.3 to 26.3 μm, while the number of small pores (<3 μm) slightly increases. The total intruded pore volume is reduced to 1544 mm^3/g.

All samples fabricated in water display lamellar pores aligned parallel to the freezing direction (Fig. 10). The pore size and the wall thickness decrease with increasing cooling rate; a large number of bridges between the walls found in these specimens is desirable for stiffening and strengthening the materials. The pore size distribution and the pore volume for specimen frozen with 6 °C/min is

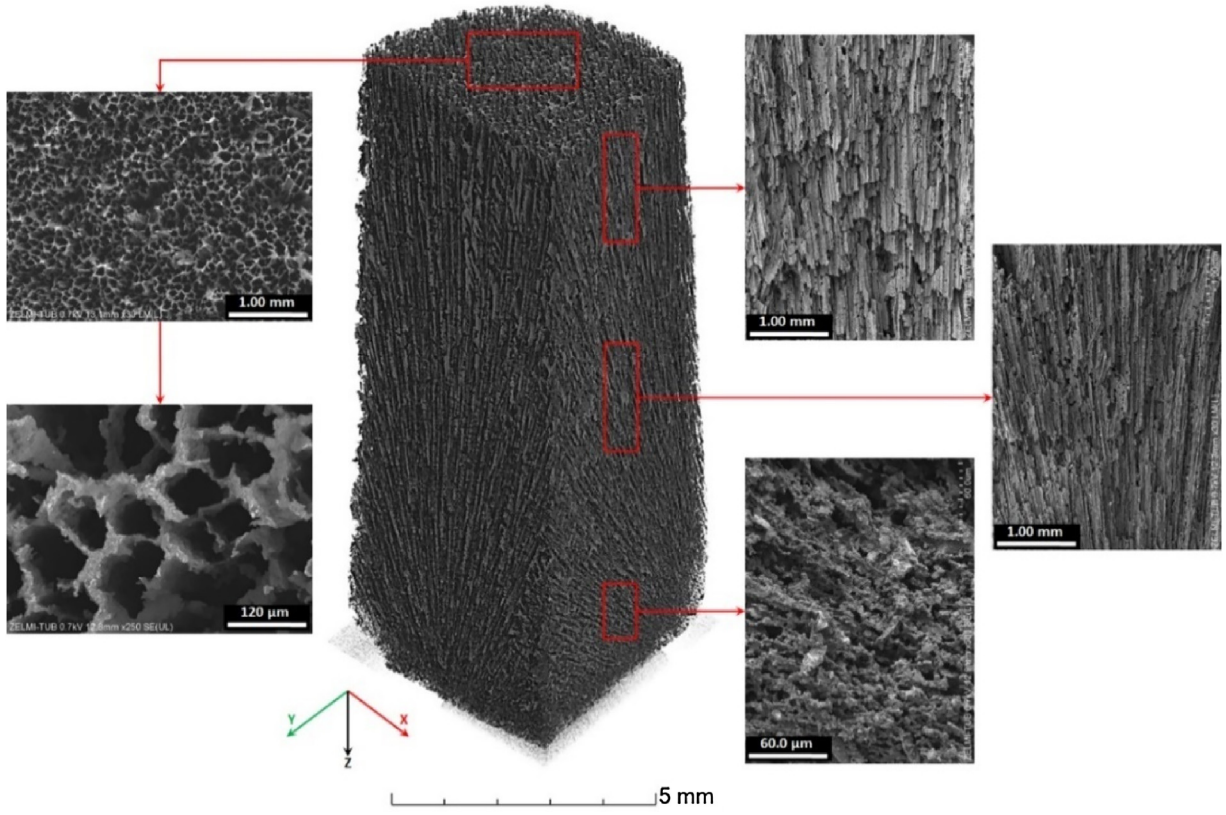

Fig. 8. Hexagonal pore channels in L11T monolith pyrolyzed at 1100 °C. Left: SEM images with different magnification of the L11T specimen frozen with 4 °C/min. The images are taken from the surface of the specimens cut perpendicular to the freezing direction. Middle: X-ray micro-tomogram of the L11T specimen frozen with 4 °C/min. Right: SEM images of the L11T specimen frozen with 2 °C/min. The images are taken from the surface of the samples taken at the positions indicated in the tomogram parallel to the freezing direction. It should be noted that these images just show the pore morphology regarding to the type of solvent and the position where the photos are taken. The pore size changes depending to the cooling rate.

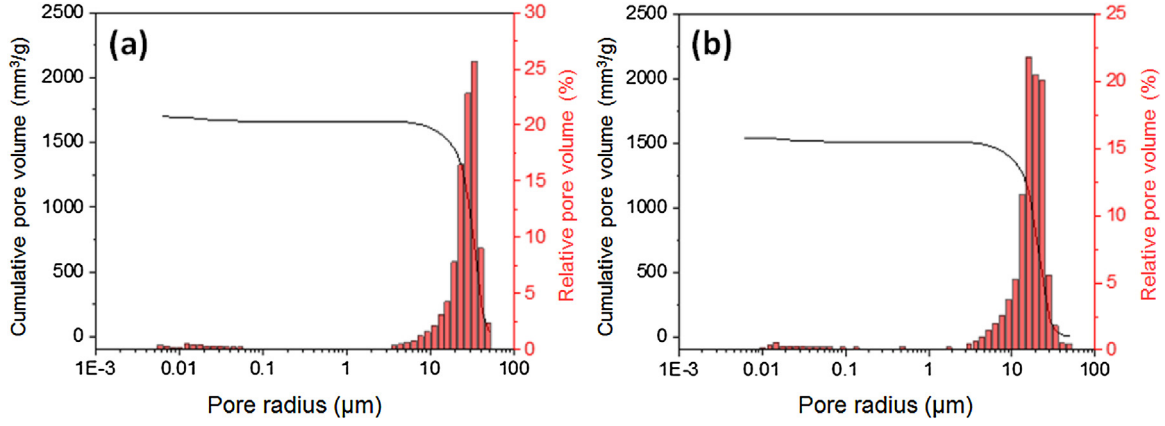

Fig. 9. Mercury intrusion porosimetry results: pore size distribution and pore volume in the L11T monoliths frozen with a) 2 and b) 6 °C/min and pyrolyzed at 1100 °C.

shown in Fig. 11. Most of the pore radii range between 0.01–30 µm with a median radius of 5.4 µm and a total intruded pore volume of 2408 mm^3/g. The increase in pore volume for water-based prepared monoliths (see also Fig. 9) is in good agreement with Deville et al. [9]. Among others, by increasing the surface tension, the breakthrough concentration and thus amount of macropores in comparison to micropores will be increased. Smaller pore sizes for water-based routes can be attributed to faster heat transfer (that effectively means higher cooling rates and freezing front velocities) due to higher thermal conductivity of water (~0.6 W/mK at 280 K [57]) if compared to TBA (~0.1 W/mK [58]).

The effect of pyrolysis temperature on the pores wall consolidation of monoliths prepared by cross-linked polymer is shown in Fig. 12. Also in this case, characteristic pore channels are observed in the samples freeze-cast in water and TBA. However, in comparison to the LH62C-based routes, the polymer crosslinking leads to more randomly oriented pores with inhomogeneously distributed micron-sized particles within the walls that make the pore walls loose, weak and unstable. The latter can be significantly strengthened in the specimens pyrolyzed at 1400 °C (Fig. 12c and d) which, however, are less porous and already phase-separated, as it will be shown below. In the next step the structure of the L11W specimens is addressed in more detail by XRD (Fig. 13), TEM (Figs. 14 and 16)

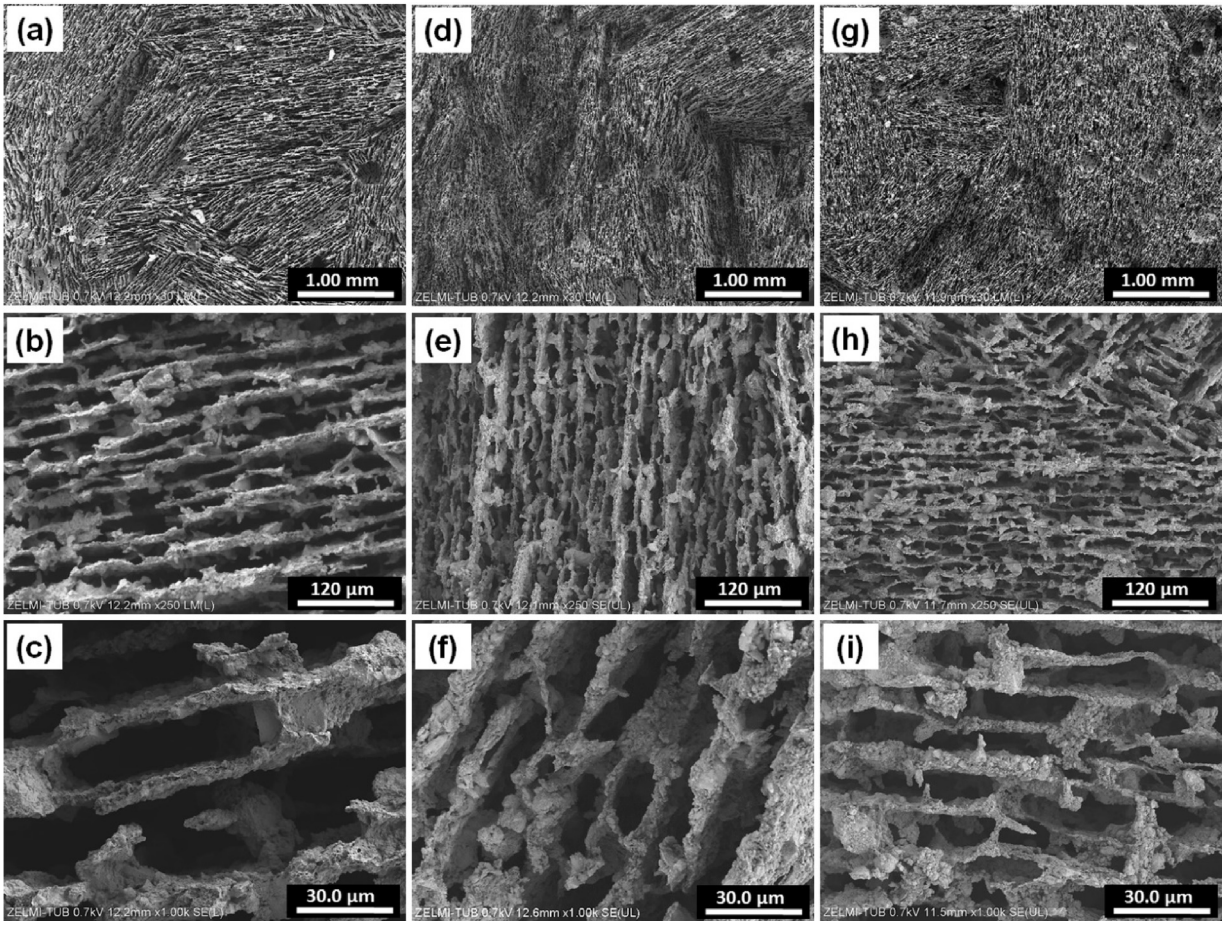

Fig. 10. Influence of cooling rate on the size of lamellar pores in the monoliths freeze-cast in water: SEM images of the L11W monoliths frozen with 2 (a-c), 4 (d-f) and 6 °C/min (g-i) and pyrolyzed at 1100 °C. The images are taken from the surface of the specimens cut parallel to the freezing direction from the same height.

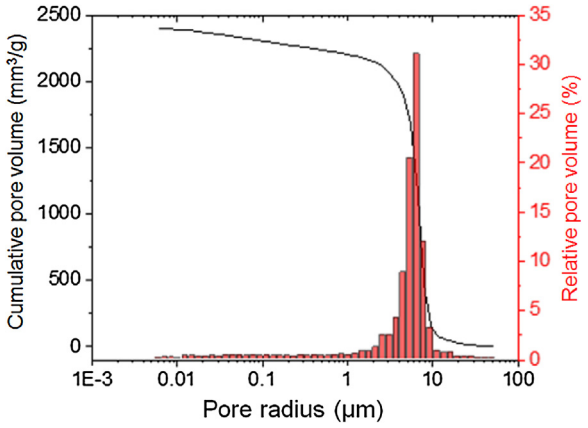

Fig. 11. Mercury intrusion porosimetry results: pore size distribution and pore volume in the L11W monoliths frozen with 6 °C/min and pyrolyzed at 1100 °C.

and NMR (Fig. 15) to identify the influence of the amorphous SiO_2 filler on the microstructure of the SiOC/SiO_2 ceramics.

According to the XRD results (Fig. 13a) the L11W sample pyrolyzed at 1100 °C remains amorphous, however, in contrast to SiOC ceramics derived from Silres H62C polymer, the TEM characterization indicates the precipitations of SiC nanocrystallites in the amorphous SiOC matrix as well as amorphous SiO_2 filler. The interplanar distance of approximately 0.25 nm corresponds to the (111) planes of β-SiC. In addition, crystalline CaO particles are observed. The latter could arise either from the impurities from the natural rice husk or from the contamination of the sample.

The XRD and TEM results point out that the polymer-derived matrix prevents the crystallization of amorphous silica particles embedded in it. Similar tendencies in the high temperature stabilization were observed for ZrO_2/SiOC and HfO_2/SiOC ceramic nanocomposites, i.e. ZrO_2 and HfO_2 particles remained amorphous after the pyrolysis in argon at 1100 and 1300 °C, respectively, and crystalized to tetragonal/cubic phases above 1300 °C [59,60]. For better resolution of the signals of the carbon containing species, solid-state ^{29}Si-NMR was performed for a L21W sample with high carbon content. The characteristic peaks observed at chemical shifts of −108 and −21 ppm correspond to SiO_4 and SiC_4 units, while −65, −31 correspond to different kinds of oxygen-rich SiC_xO_{4-x} units [54,55]. In contrast to ^{29}Si-NMR spectra of LH62C-derived SiOC sample (see Fig. 15), the intensity of SiO_4 peak of the composite is much higher in comparison to the intensities of the carbon containing Si-O-C-species, which is due to the silica filler. Furthermore, all peaks are shifted towards lower fields in comparison to the LH62C-derived SiOC. As mixed Si-C-O bonds are still observed, the amorphous SiOC matrix remains still intact and the phase-segregation into the oxygen-rich and carbon-rich units is not completed similar to the LH62C-derived SiOC specimens.

With increasing pyrolysis temperature to 1400 °C, amorphous silica particles embedded in SiOC matrix crystallizes to α-cristobalite (main phase) and β-tridymite. Similar to the LH62C-derived sample the SiOC matrix undergoes the phase separation to β-SiC and turbostratic carbon. The Rietveld refinement of the XRD pattern of the L11W sample pyrolyzed at 1400 °C (Fig. 13b)

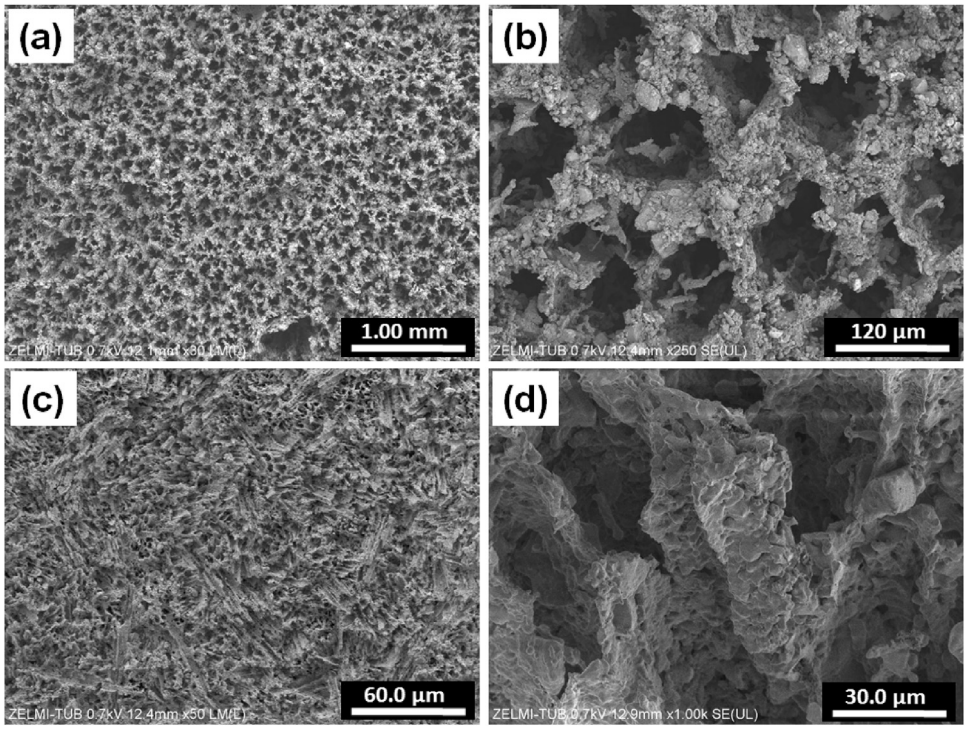

Fig. 12. Effect of pyrolysis temperature on the pores wall consolidation of cross-linked sample and phase-separation of pore structure: SEM images of the C11T monoliths frozen at 6 °C/min and pyrolyzed at 1100 (a, b) and 1400 °C (c, d). The images are taken from the surface of the specimens cut perpendicular to the freezing direction.

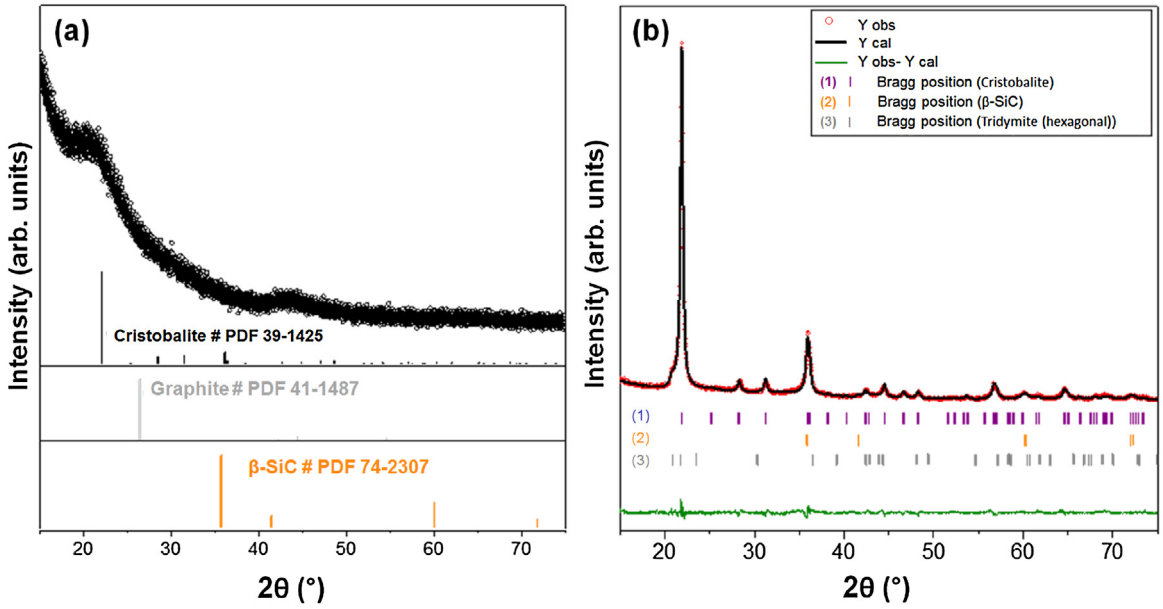

Fig. 13. XRD pattern of (a) L11W sample pyrolyzed at 1100 °C; (b) Rietveld refinement of L11W sample pyrolyzed at 1400 °C, showing observed (red circles), calculated (black solid line) intensities and difference (green solid line). Tick marks refer to Bragg reflections of α-cristobalite SiO_2 (1), (2), β-SiC (2) and (3) hexagonal β-tridymite. (For interpretation of the references to colour in this figure legend, the reader is referred to the web version of this article.)

displays the silica is the main crystalline phase with 84.4 wt.% of α-cristobalite with crystallite sizes of 19.6 nm and 1.1 wt.% of β-tridymite with crystallite sizes of 13.1 nm β-SiC phase with crystallite sizes of 3.9 nm is of about 14.6 wt.%. The dark-field TEM images confirm the formation of nano-sized crystals in the amorphous matrix similar to the LH62C-derived SiOC specimen; the Fourier-transformed high-resolution TEM data and electron diffraction analysis confirm the nano-sized SiC crystallites with a measured interplanar distance of approximately 0.245 nm which correspond to the (111) planes of β-SiC polymorph. In addition, turbostratic carbon precipitates with interplanar distances of 0.355 nm and crystallite sizes of a few nanometers are observed. Graphite, which is observed by TEM, could not be confirmed by XRD, probably because the graphite reflections are overlapped

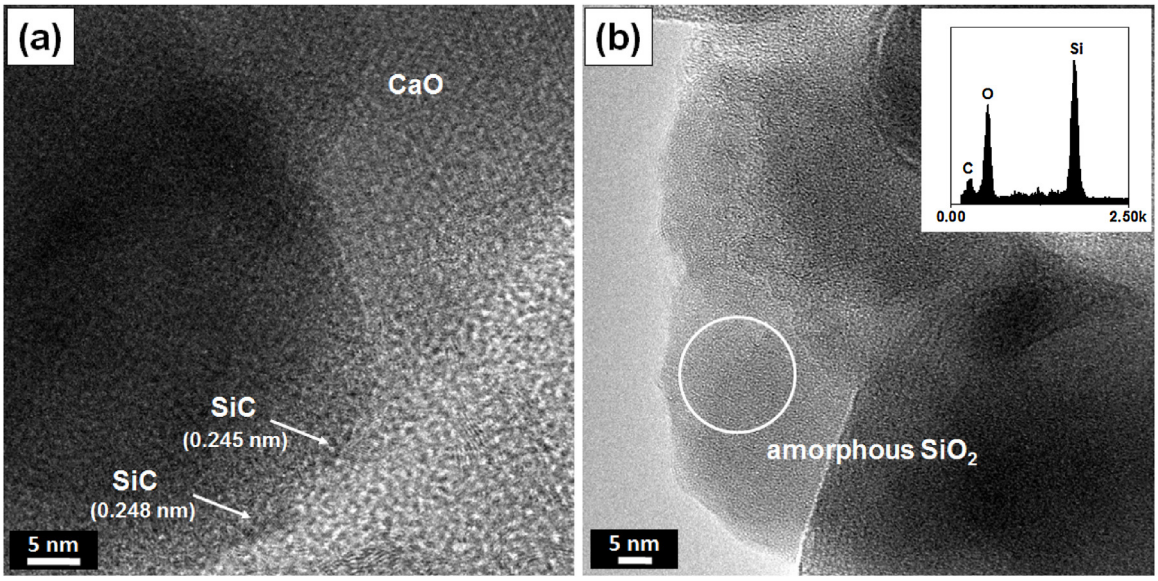

Fig. 14. HR-TEM images of L11W sample pyrolyzed at 1100 °C display tiny crystallites of β-SiC and crystalline CaO (a). In (b) the amorphous silica particle with the corresponding EDX spectra is shown.

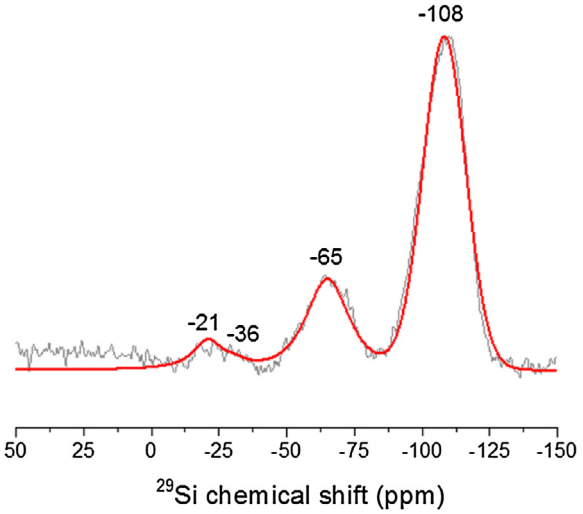

Fig. 15. Solid-state $^{29}Si\{^{1}H\}$-NMR spectrum of L21W sample pyrolyzed at 1100 °C. See the text for the interpretation of the spectra.

by highly intense reflections of the crystalline SiO_2 phases. The TEM images display also monocrystalline SiO_2 (probably tridymite phase), which were not observed in the LH62C-derived SiOC specimen, crystallized during pyrolysis from the amorphous silica filler. No indication was found, that crystalline silica is formed out of the SiOC matrix itself. As known, SiO_2 crystallization from the amorphous SiOC matrix in polymer derived ceramics is inhibited, i.e. cristobalite was observed in for SiOC PDCs only for long term annealing times at temperatures between 1300 and 1400 °C [61]. In the SiOC matrix carbon impedes the required breaking up of Si—O—C bonds and hinders the diffusion and rearrangement of atoms to crystalline silica structures.

4. Conclusions

We successfully fabricated polymer-derived macroporous amorphous SiOC/SiO_2 monoliths with aligned pore channels by freeze-casting techniques using water and tert-butyl alcohol as solvents. A commercially available methyl-phenyl-vinyl-hydrogen polysiloxane (Silres® H62C) was applied as preceramic polymer. Amorphous silica obtained from rice husk ash was used as a filler to reduce shrinkage of polymer-derived ceramics and enhance the form stability of the final monoliths. The pre-crosslinking of the polysiloxane before the freeze-casting process also reduces shrinkage but leads to inhomogeneous cell walls and thus to lower mechanical strength of the monoliths which can be improved by sintering at higher pyrolysis temperatures. By varying the cooling rate the pores can be tailored in size, i.e. slow cooling rates lead to large pores. To make the processing route more environmentally friendly, the freeze-casting process was adapted to water-based microemulsions of polysiloxane with silica. Water-based freeze-casting leads to characteristic lamellar pore structures. Monoliths with a polymeric ratio to silica of 1:1 were analyzed in detail. While tert-butyl alcohol based processing route leads to a pore radius distribution mainly in the range of 3 μm–50 μm with a median pore size radius of 16.3 μm and a total intruded pore volume of 1719 mm^3/g, water leads to finer pores with broad pore radius distribution between 0.01–30 μm and a median pore radius of 5.4 μm and a total intruded pore volume of 2408 mm^3/g. Complementary XRD, solid-state NMR and TEM characterizations were performed for the ceramic nanocomposites as well as for the pure polymer-derived SiOC ceramics for comparison. After pyrolysis at 1100 °C both materials are X-ray amorphous. Interestingly, silica filler stays amorphous within the polymer-derived matrix, although crystallization for the pure silica is already observed at this temperature. Thus, free carbon within the polymer-derived matrix hinders not only the phase segregation and crystallization within the SiOC matrix, but also of amorphous particles dispersed in it. After pyrolysis at 1400 °C SiOC matrix segregation in oxygen-rich and carbon-rich SiC_xO_{4-x} units takes place. XRD and TEM show nanocrystalline β-SiC and turbostratic carbon phases in the range of 1–2 nm. In the nanocomposite, crystallization of the amorphous silica filler to cristobalite and tridymite phases is observed along with crystal growth of the silica phase.

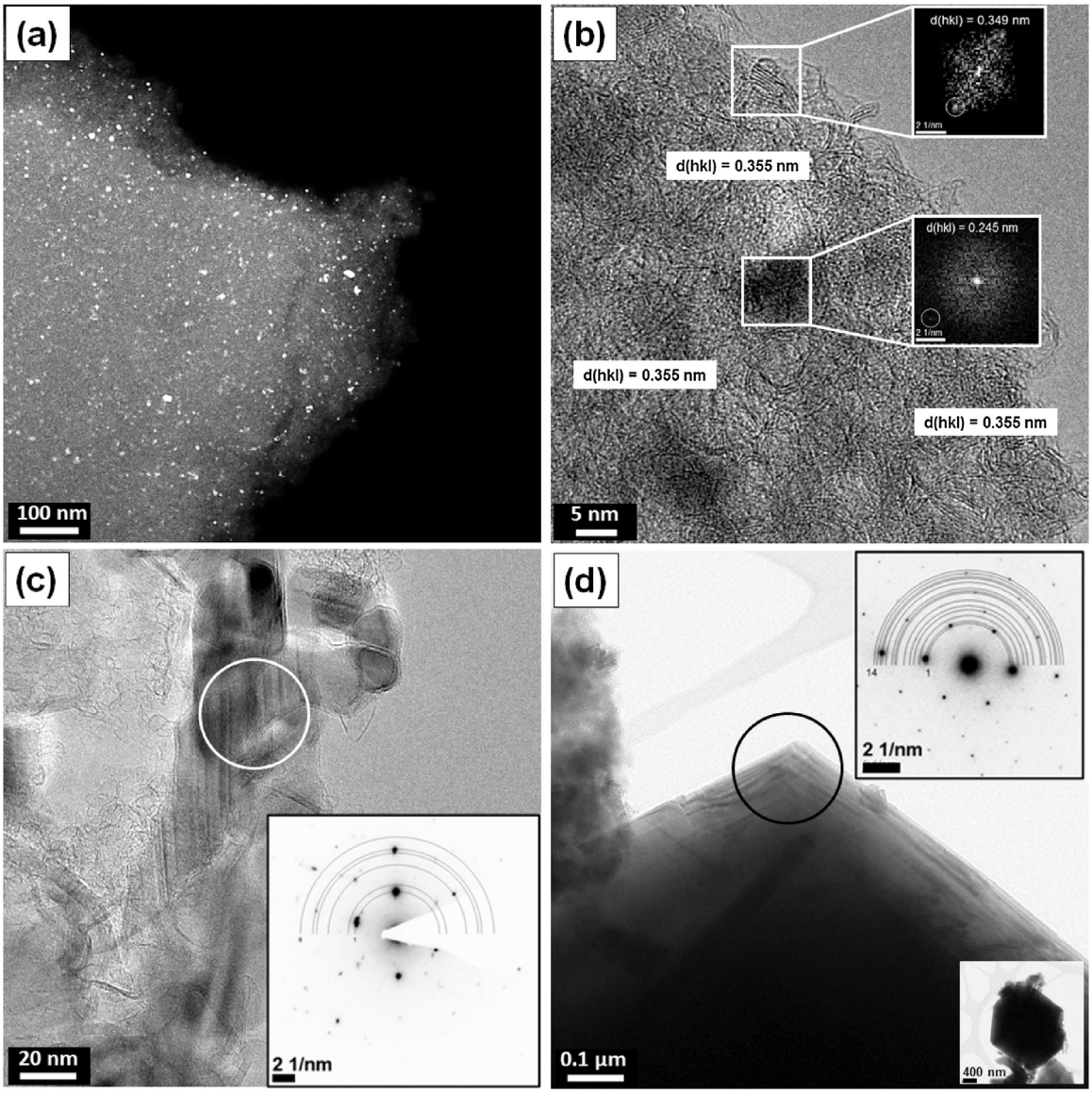

Fig. 16. L11W sample pyrolyzed at 1400 °C: a) dark field TEM image displays tiny crystals within the amorphous matrix, b) HR-TEM show β-SiC nanocrystals with interplanar distances of approximately 0.245 nm that correspond to (111) planes (inset shows Fourier-transformed high-resolution TEM data) and turbostratic carbon with interplanar distances of 0.355 nm (inset shows Fourier-transformed high resolution TEM data); c) besides homogenous crystals unordered parts can be seen which correspond to β-SiC (inset: diffraction pattern of β-SiC, see Table S1 for details); d) SiO_2 crystals (probably tridymite phase) crystallized from the amorphous silica filler are depicted (insets: TEM image with lower magnification and corresponding diffraction pattern, see Table S1 for details).

Acknowledgement

Niloofar Soltani and Amin Bahrami gratefully acknowledge PAPIIT-DGAPA for granting a postdoctoral scholarship in Material Research Institute of National Autonomous University of Mexico (IIM-UNAM), and also, CONACYT (National Council of Science and Technology, in Mexico) for granting an academic stay scholarship in Technische Universität Berlin. U. S. and A. G. thank the Cluster of Excellence "Unifying Concepts in Catalysis" for funding. The project was partially financed by the German Research Foundation (DFG −Deutsche Forschungsgemeinschaft) under the grant GU992/17-1. The authors are also thankful to Mr. Ulrich Gernert (ZELMI, Technische Universität Berlin) and Paul H. Kamm for SEM and μ-CT characterization; respectively. Technical assistance of Sara Zavareh at the freeze-casting setup is also acknowledged.

Appendix A. Supplementary data

Supplementary data associated with this article can be found, in the online version, at http://dx.doi.org/10.1016/j.jeurceramsoc.2017.06.023.

References

[1] R. Liu, T. Xu, C.-A. Wang, A review of fabrication strategies and applications of porous ceramics prepared by freeze-casting method, Ceram. Int. 42 (2016) 2907–2925 (2, Part B).
[2] M. Seifollahi Bazarjani, M.M. Müller, H.-J. Kleebe, Y. Jüttke, I. Voigt, M. Baghaie Yazdi, L. Alff, R. Riedel, A. Gurlo, High-temperature stability and saturation magnetization of superparamagnetic nickel nanoparticles in microporous polysilazane-derived ceramics and their gas permeation properties, ACS Appl. Mater. Interfaces 6 (15) (2014) 12270–12278.
[3] E.C. Hammel, O.L.R. Ighodaro, O.I. Okoli, Processing and properties of advanced porous ceramics: an application based review, Ceram. Int. 40 (2014) 15351–15370 (10, Part A).
[4] C. Vakifahmetoglu, D. Zeydanli, P. Colombo, Porous polymer derived ceramics, Mater. Sci. Eng. R: Rep. 106 (2016) 1–30.

[5] K. Lu, Porous and high surface area silicon oxycarbide-based materials—a review, Mater. Sci. Eng. R: Rep. 97 (2015) 23–49.
[6] S. Deville, Freeze-Casting of porous ceramics: a review of current achievements and issues, Adv. Eng. Mater. 10 (3) (2008) 155–169.
[7] L. Qian, H. Zhang, Controlled freezing and freeze drying: a versatile route for porous and micro-/nano-structured materials, J. Chem. Technol. Biot. 86 (2) (2011) 172–184.
[8] S. Deville, E. Maire, G. Bernard-Granger, A. Lasalle, A. Bogner, C. Gauthier, J. Leloup, C. Guizard, Metastable and unstable cellular solidification of colloidal suspensions, Nat. Mater. 8 (12) (2009) 966–972.
[9] S. Deville, G. Bernard-Granger, Influence of surface tension, osmotic pressure and pores morphology on the densification of ice-templated ceramics, J. Eur. Ceram. Soc. 31 (6) (2011) 983–987.
[10] H. Bai, Y. Chen, B. Delattre, A.P. Tomsia, R.O. Ritchie, Bioinspired large-scale aligned porous materials assembled with dual temperature gradients, Sci. Adv. 1 (11) (2015).
[11] W.L. Li, K. Lu, J.Y. Walz, Freeze casting of porous materials: review of critical factors in microstructure evolution, Int. Mater. Rev. 57 (1) (2012) 37–60.
[12] S. Blindow, M. Pulkin, D. Koch, G. Grathwohl, K. Rezwan, Hydroxyapatite/SiO2 composites via freeze casting for bone tissue engineering, Adv. Eng. Mater. 11 (11) (2009) 875–884.
[13] A. Ojuva, F. Akhtar, A.P. Tomsia, L. Bergström, Laminated adsorbents with very rapid CO2 uptake by freeze-casting of zeolites, ACS Appl. Mater. Interfaces 5 (7) (2013) 2669–2676.
[14] P. Colombo, G. Mera, R. Riedel, G.D. Sorarù, Polymer-derived ceramics: 40 years of research and innovation in advanced ceramics, J. Am. Ceram. Soc. 93 (7) (2010) 1805–1837.
[15] R.M. Prasad, G. Mera, K. Morita, M. Müller, H.-J. Kleebe, A. Gurlo, C. Fasel, R. Riedel, Thermal decomposition of carbon-rich polymer-derived silicon carbonitrides leading to ceramics with high specific surface area and tunable micro- and mesoporosity, J. Eur. Ceram. Soc. 32 (2) (2012) 477–484.
[16] C. Schitco, M.S. Bazarjani, R. Riedel, A. Gurlo, NH3-assisted synthesis of microporous silicon oxycarbonitride ceramics from preceramic polymers: a combined N2 and CO2 adsorption and small angle X-ray scattering study, J. Mater. Chem. A 3 (2) (2015) 805–818.
[17] Y. Grebenyuk, H. Zhang, M. Wilhelm, K. Rezwan, M. Dreyer, Wicking into porous polymer-derived ceramic monoliths fabricated by freeze-casting, J. Eur. Ceram. Soc. 37 (5) (2017) 1993–2000.
[18] M. Naviroj, M.M. Wang, M.T. Johnson, K.T. Faber, Nucleation-controlled freeze casting of preceramic polymers for uniaxial pores in Si-based ceramics, Scr. Mater. 130 (2017) 32–36.
[19] B.H. Yoon, E.J. Lee, H.E. Kim, Y.H. Koh, Highly aligned porous silicon carbide ceramics by freezing polycarbosilane/camphene solution, J. Am. Ceram. Soc. 90 (6) (2007) 1753–1759.
[20] M. Naviroj, S. Miller, P. Colombo, K. Faber, Directionally aligned macroporous SiOC via freeze casting of preceramic polymers, J. Eur. Ceram. Soc. 35 (8) (2015) 2225–2232.
[21] H. Zhang, P.D.A. Nunes, M. Wilhelm, K. Rezwan, Hierarchically ordered micro/meso/macroporous polymer-derived ceramic monoliths fabricated by freeze-casting, J. Eur. Ceram. Soc. 36 (1) (2016) 51–58.
[22] H. Zhang, P. D'Angelo Nunes, M. Wilhelm, K. Rezwan, Hierarchically ordered micro/meso/macroporous polymer-derived ceramic monoliths fabricated by freeze-casting, J. Eur. Ceram. Soc. 36 (1) (2016) 51–58.
[23] N. Soltani, A. Bahrami, M.I. Pech-Canul, L.A. González, Review on the physicochemical treatments of rice husk for production of advanced materials, Chem. Eng. J. 264 (2015) 899–935.
[24] O. Goerke, E. Feike, H. Schubert, Spray winding, a novel one-step spray-technology to perform CMCs from preceramic polymers, J. Eur. Ceram. Soc. 25 (2–3) (2005) 181–185.
[25] A. Bahrami, M.I. Pech-Canul, C.A. Gutiérrez, N. Soltani, Wetting and reaction characteristics of crystalline and amorphous SiO2 derived rice-husk ash and SiO2/SiC substrates with Al–Si–Mg alloys, Applied Surface Science 357, Appl. Surf. Sci. 357 (2015) 1104–1113, Part A.
[26] A. Bahrami, N. Soltani, M.I. Pech-Canul, C.A. Gutiérrez, Development of metal-matrix composites from industrial/agricultural waste materials and their derivatives, Crit. Rev. Environ. Sci. Technol. 46 (2) (2016) 143–208.
[27] N. Soltani, S. Soltani, A. Bahrami, M.I. Pech-Canul, L.A. Gonzalez, A. Möller, J. Tapp, A. Gurlo, Electrical and thermomechanical properties of CVI- Si3N4 porous rice husk ash infiltrated by Al-Mg-Si alloys, J. Alloys Compd. 696 (2017) 856–868.
[28] A. Bahrami, U. Simon, N. Soltani, S. Zavareh, J. Schmidt, M.I. Pech-Canul, A. Gurlo, Eco-fabrication of hierarchical porous silica monoliths by ice-templating of rice husk ash, Green Chem. 19 (1) (2017) 188–195.
[29] S. Zavareh, A. Hilger, K, O. Hirselandt, I. Goerke, J. Manke, A. Banhart, Gurlo, Fabrication of cellular and lamellar LiFePO4/C Cathodes for Li-ion batteries by unidirectional freeze-casting method, J. Ceram. Soc. Jpn. 124 (10) (2016) 1067–1071.
[30] F. García Moreno, M. Fromme, J. Banhart, Real-time X-ray radioscopy on metallic foams using a compact micro-focus source, Adv. Eng. Mater. 6 (6) (2004) 416–420.
[31] J. Rodriguez-Carvajal, FULLPROF: a Program for Rietveld Refinement and Pattern Matching Analysis, Satellite Meeting on Powder Diffraction of the XV Congress of the IUCr, Toulouse France :[sn], 1990.
[32] L.W. Finger, D.E. Cox, A.P. Jephcoat, A correction for powder diffraction peak asymmetry due to axial divergence, J. Appl. Crystallogr. 27 (6) (1994) 892–900.
[33] D. Massiot, F. Fayon, M. Capron, I. King, S. Le Calvé, B. Alonso, J.-O. Durand, B. Bujoli, Z. Gan, G. Hoatson, Modelling one- and two-dimensional solid-state NMR spectra, Magn. Reson. Chem. 40 (1) (2002) 70–76.
[34] R. Gadow, F. Kern, H. Ulutas, Mechanical properties of ceramic matrix composites with siloxane matrix and liquid phase coated carbon fiber reinforcement, J. Eur. Ceram. Soc. 25 (2–3) (2005) 221–225.
[35] O. Goerke, E. Feike, T. Heine, A. Trampert, H. Schubert, Ceramic coatings processed by spraying of siloxane precursors (polymer-spraying), J. Eur. Ceram. Soc. 24 (7) (2004) 2141–2147.
[36] M. Woiton, M. Heyder, A. Laskowsky, E. Stern, M. Scheffler, C.J. Brabec, Self-assembled microstructured polymeric and ceramic surfaces, J. Eur. Ceram. Soc. 31 (9) (2011) 1803–1810.
[37] H. Elsayed, M. Sinico, M. Secco, F. Zorzi, P. Colombo, E. Bernardo, B-doped hardystonite bioceramics from preceramic polymers and fillers: synthesis and application to foams and 3D-printed scaffolds, J. Eur. Ceram. Soc. 37 (4) (2017) 1757–1767.
[38] R.M. Rocha, J.C. Bressiani, A.H.A. Bressiani, Ceramic substrates of β-SiC/SiAlON composite from preceramic polymers and Al–Si fillers, Ceram. Int. 40 (9) (2014) 13929–13936, Part A.
[39] A. Francis, R. Detsch, A.R. Boccaccini, Fabrication and cytotoxicity assessment of novel polysiloxane/bioactive glass films for biomedical applications, Ceram. Int. 42 (14) (2016) 15442–15448.
[40] L. Fiocco, E. Bernardo, Novel cordierite foams from preceramic polymers and reactive oxide fillers, Mater. Lett. 159 (2015) 98–101.
[41] G. Parcianello, E. Bernardo, P. Colombo, Low temperature synthesis of zircon from silicone resins and oxide nano-sized particles, J. Eur. Ceram. Soc. 32 (11) (2012) 2819–2824.
[42] R. Falgenhauer, P. Rambacher, L. Schlier, J. Volkert, N. Travitzky, P. Greil, M. Weclas, Electrically heated 3D-macro cellular SiC structures for ignition and combustion application, Appl. Therm. Eng. 112 (2017) 1557–1565.
[43] Z. Fu, L. Schlier, N. Travitzky, P. Greil, Three-dimensional printing of SiSiC lattice truss structures, Mater. Sci. Eng.: A 560 (2013) 851–856.
[44] F. Kern, R. Gadow, Deposition of ceramic layers on carbon fibers by continuous liquid phase coating, Surf. Coat. Technol. 180–181 (2004) 533–537.
[45] E. Bernardo, P. Colombo, E. Dainese, G. Lucchetta, P.F. Bariani, Novel 3D wollastonite-based scaffolds from preceramic polymers containing micro- and nano-Sized reactive particles, Adv. Eng. Mater. 14 (4) (2012) 269–274.
[46] M. Thünemann, Poröse SiC-Keramiken Mittels Präkeramischer Polymere, Fachhochschule Münster, Germany, 2003.
[47] Z.Q. Li, C.J. Lu, Z.P. Xia, Y. Zhou, Z. Luo, X-ray diffraction patterns of graphite and turbostratic carbon, Carbon 45 (8) (2007) 1686–1695.
[48] Z.-M. Gao, H.-Z. Jin, X.-S. Li, Z. Hua, Phase transformation mechanism of graphite-turbostratic graphite in the course of mechanical grinding, Chem. Res. Chin. Univ. 19 (2) (2003) 216–218.
[49] K.J. Kim, J.-H. Eom, T.Y. Koh, Y.-W. Kim, W.-S. Seo, Effects of carbon addition on the electrical properties of bulk silicon-oxycarbide ceramics, J. Eur. Ceram. Soc. 36 (11) (2016) 2705–2711.
[50] H.D. Akkaş, M.L. Öveçoğlu, M. Tanoğlu, Silicon oxycarbide-based composites produced from pyrolysis of polysiloxanes with active Ti filler, J. Eur. Ceram. Soc. 26 (15) (2006) 3441–3449.
[51] G. Mera, A. Navrotsky, S. Sen, H.-J. Kleebe, R. Riedel, Polymer-derived SiCN and SiOC ceramics – structure and energetics at the nanoscale, J. Mater. Chem. A 1 (12) (2013) 3826–3836.
[52] H. Takagi, K. Maruyama, N. Yoshizawa, Y. Yamada, Y. Sato, XRD analysis of carbon stacking structure in coal during heat treatment, Fuel 83 (17–18) (2004) 2427–2433.
[53] H. Störmer, H.-J. Kleebe, G. Ziegler, Metastable SiCN glass matrices studied by energy-filtered electron diffraction pattern analysis, J. Non-Cryst. Solids 353 (30–31) (2007) 2867–2877.
[54] T. Xu, Q. Ma, Z. Chen, High-temperature behavior of silicon oxycarbide glasses in air environment, Ceram. Int. 37 (7) (2011) 2555–2559.
[55] C. Schiţco, C. Turdean-Ionescu, M.S. Bazarjani, C.-W. Tai, D. Li, C. Fasel, W. Donner, J. Shen, R. Riedel, A. Gurlo, M. Edén, Silicon oxycarbonitrides synthesized by ammonia-assisted thermolysis route from polymers: a total X-ray scattering, solid-state NMR, and TEM structural study, J. Eur. Ceram. Soc. 36 (4) (2016) 979–989.
[56] L. Hu, C.-A. Wang, Y. Huang, C. Sun, S. Lu, Z. Hu, Control of pore channel size during freeze casting of porous YSZ ceramics with unidirectionally aligned channels using different freezing temperatures, J. Eur. Ceram. Soc. 30 (16) (2010) 3389–3396.
[57] P.E. Liley, T. Makita, Y. Tanaka, Properties of Inorganic and Organic Fluids, Taylor & Francis, 2016.
[58] 1999. https://cameochemicals.noaa.gov/chris/BAT.pdf.
[59] E. Ionescu, C. Linck, C. Fasel, M. Müller, H.J. Kleebe, R. Riedel, Polymer-Derived SiOC/ZrO2 ceramic nanocomposites with excellent high-temperature stability, J. Am. Ceram. Soc. 93 (1) (2010) 241–250.
[60] E. Ionescu, B. Papendorf, H.-J. Kleebe, R. Riedel, Polymer-derived silicon Oxycarbide/Hafnia ceramic nanocomposites. part II: stability toward decomposition and microstructure evolution at $T \gg 1000\,^{\circ}C$, J. Am. Ceram. Soc. 93 (6) (2010) 1783–1789.
[61] G. Mera, M. Gallei, S. Bernard, E. Ionescu, Ceramic nanocomposites from tailor-made preceramic polymers, Nanomaterials 5 (2) (2015) 468.